Ultrasonics Sonochemistry 92 (2023) 106272

Contents lists available at ScienceDirect

Ultrasonics Sonochemistry

journal homepage: www.elsevier.com/locate/ultson

In situ measurement of cavitation damage from single bubble collapse using high-speed chronoamperometry

Morteza Abedini [a,b,*], Stefanie Hanke [b], Fabian Reuter [c,*]

[a] Department of Metallurgy and Materials Engineering, Faculty of Engineering, University of Kashan, Kashan, Iran
[b] Materials Science and Engineering, Institute for Metal Technologies, University Duisburg-Essen, 47057 Duisburg, Germany
[c] Department Soft Matter, Institute for Physics, Faculty of Natural Sciences, Otto-von-Guericke University Magdeburg, Universitätsplatz 2, 39106 Magdeburg, Germany

ARTICLE INFO

Keywords:
Cavitation
Corrosion
Erosion
Chronoamperometry
Bubble Dynamics

ABSTRACT

We quantitatively study cavitation damage non-invasively, in-place and time-resolved at microsecond resolution. A single, laser-induced bubble is generated in an aqueous NaCl solution close to the surface of an aluminum sample. High-speed chronoamperometry is used to record the corrosion current flowing between the sample and an identical aluminum electrode immersed in the same solution. This configuration makes it possible to measure the cavitation damage in the nanometer thin passive layer of the aluminum surface via the corrosion current from the repassivation. Synchronously with the corrosion current, the bubble dynamics is recorded via high-speed imaging. Correlation between the two measurements allows contributing cavitation damage to the respective stages of the bubble dynamics. The largest cavitation-induced currents were observed for the smallest initial bubble-to-surface stand-off distances. As the bubble re-expands and collapses again in several stages, further current peaks were detected implying a sequence of smaller damage. At intermediate stand-offs the bubble was not damaging and at large stand-off distances, the bubble was only damaging during the second collapse which again occurs at the solid surface.

1. Introduction

Cavitation refers to the formation and collapse of bubbles in a liquid due to pressure changes. When the bubble collapse occurs near a solid boundary, the solid surface experiences significant stresses resulting in material damage. The surface can be plastically deformed, and the material can even detach from hard steel surfaces. This is known as cavitation erosion. Numerous technical systems with hydrodynamic and acoustic cavitation experience cavitation erosion. A standard test procedure to estimate the cavitation erosion resistance of materials is given by ASTM G32 [1] according to which an ultrasonic horn induces cavitation in a small millimeter-sized gap of water between the horn surfaces and the material to be tested. The weight loss by cavitation erosion after a certain period of sonication is measured by ex-situ weighing before and after exposure to cavitation. The mass loss rate depends on the sonication time, as the sample surface structure is altered during the erosion process. Here the cavitation appears in large bubble clouds in a small gap, therefore, the study of damage details using high-speed imaging is hardly feasible.

Instead, the mechanisms of cavitation erosion were studied employing single bubble collapses at flat solid samples employing either spark induced or optic cavitation. The ground laying works by Shutler [2], Shima [3], Philipp and Lauterborn [4] and Isselin et al. [5] showed that the bubble dynamics and the resulting damage crucially depend on the bubble to wall stand-off. The bubble to wall stand-off is commonly expressed in non-dimensional form as $\gamma = d/R_{max}$, where γ is the stand-off parameter, d is the distance of the bubble center to the solid surface and R_{max} is the maximum bubble radius. In these studies, the cavitation damage was mainly studied ex-situ using surface profilometry of the eroded samples. They triggered many further studies aiming to elucidate the cavitation erosion mechanism on hard materials [2–5]. Recently, it was found that an additional energy-focusing mechanism is required for erosive cavitation. For smallest bubble to wall stand-offs, the bubble collapse is amplified by a shockwave self-focusing mechanism that drives an erosive collapse of part of the gas phase and produces erosion away from the axis of symmetry. This has been shown to be the only significant mechanism behind cavitation erosion which is able to generate visible damage already after a single bubble impact on hard metal surfaces, without fatigue at play [6]. In the later work the damage detection could be done in-situ but required specialized imaging

* Corresponding authors at: Department of Metallurgy and Materials Engineering, Faculty of Engineering, University of Kashan, Kashan, Iran (M. Abedini).
E-mail addresses: morteza.abedini@uni-due.de (M. Abedini), fabian.reuter@ovgu.de (F. Reuter).

https://doi.org/10.1016/j.ultsonch.2022.106272
Received 2 September 2022; Received in revised form 17 December 2022; Accepted 19 December 2022
Available online 20 December 2022
1350-4177/© 2022 Published by Elsevier B.V. This is an open access article under the CC BY-NC-ND license (http://creativecommons.org/licenses/by-nc-nd/4.0/).

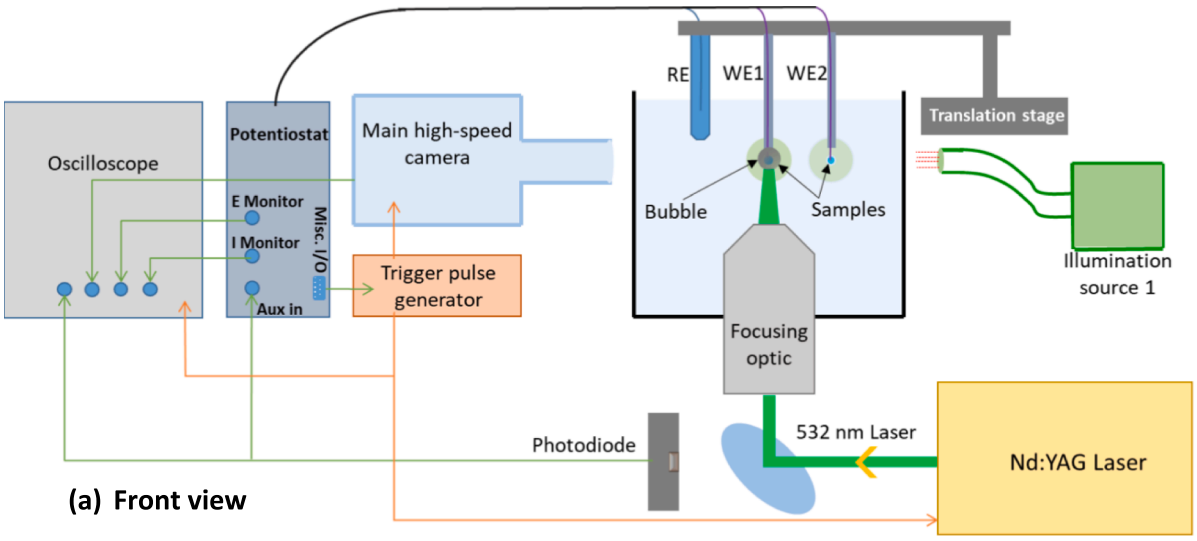

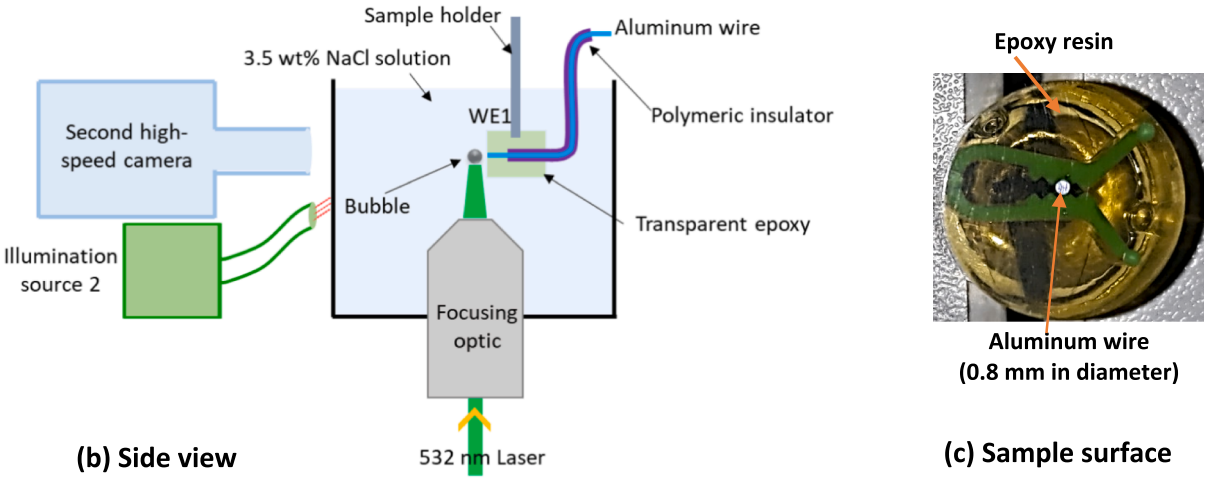

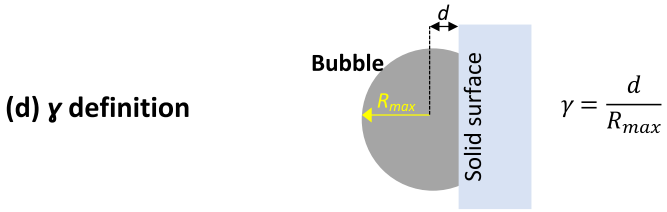

Fig. 1. Experimental setup: (a) front view and (b) side view. Figure c shows the surface of aluminum sample embedded in the epoxy resin. The bubble radius at maximum expansion R_{max}, and the stand-off distance are defined in Figure d.

equipment and the damage quantification relied on ex-situ measurements.

Besides the optical techniques, electrochemical methods can detect and quantify cavitation damage in-situ. Polarization method and electrochemical impedance spectrometry (EIS) are the two most common electrochemical methods in the corrosion studies. These two methods have been widely used to quantify the effect of cavitation erosion on corrosion and vice versa [7–12]. However, insensitivity to high-speed short-time changes on the surface, makes these two methods not suitable for the study of cavitation damage under single bubble collapse which occurs in microsecond time-scales. Cavitation erosion increases the corrosion rate of materials mainly by enhancing the mass transfer rate of oxygen and erosive removal of corrosion products from the surface [10]. Therefore, the anodic reaction ($M \rightarrow M^{n+} + ne$, where M is metal and n is the number of electrons) on the metal surface is accelerated which means a larger number of electrons traveling from the surface at a specified time, i.e., a higher corrosion current. Measuring the corrosion rate of metals under cavitation erosion can reveal the cavitation damage on the surface, e.g., the removal of the passive layer. Some other electrochemical methods have been developed based on monitoring the time-dependent corrosion current and corrosion potential. Using these time domain methods, it is possible to record the time-dependent corrosion current with or without an applied potential. These techniques have been used to detect and quantify the damage induced

by the impingement of solid particles on the surface of samples during slurry erosion [13–15]. There are also a few works on high-speed recording of electrochemical current under single bubble cavitation synchronously with high-speed imaging to measure the wall shear rates [16] and the effect on rigid surfaces by ultrasonic cavitation [17–28]. These implementations were, however, invasive as an external potential was applied to the metal surface to increase the small corrosion current. The external perturbation can also change the corrosion rate and the passivation behavior of the metal, and the mechanical properties such as the cavitation erosion resistance may alter.

Here, we use high-speed chronoamperometry to record the time-dependent current between two identical metal samples (one of them under single bubble collapse) without any external excitation voltage. This technique allows a non-invasive in-situ study of cavitation under single bubble collapse that is correlated with the synchronous high-speed imaging of the bubble dynamics.

2. Experimental procedure and methods

Here we measure the time-resolved corrosion current during the dynamics of a laser-induced single bubble collapsing close to an aluminum surface. The corrosion current is then correlated to synchronized high-speed imaging of the bubble shape dynamics. Via the corrosion current, damage on the aluminium surface can be monitored in high temporal resolution and in-situ. The corrosion of aluminium is mainly controlled by the passive layer behaviour. On the aluminium sample surface, naturally an oxide layer with a thickness of a few nanometers is present [29–31]. If the passive layer gets sufficiently damaged, a bare surface of aluminium gets exposed to the corrosive medium. Then, the surface is quickly oxidized by the following anodic reaction $Al \rightarrow Al^{+3} + 3e^{-}$ resulting in the time-dependent current. In the course of this process, again an oxide layer forms, i.e., the sample repassivates resulting in a decrease in the current to zero within tens to hundreds of microseconds.

As sample surface the circular cross sections of 99.98% pure aluminum wires are used. Wires with a diameter of 0.8 mm were electrically insulated using heat shrink rubber tubes. The shielded wires were then embedded in transparent epoxy resin to provide a sufficiently large and plane boundary at which the bubble collapses (see Fig. 1c). They were ground with 200, 800 and 1200 grit abrasive papers and subsequently polished using 9 and 3 μm diamond suspensions and 0.02 μm alumina suspension. This resulted in an average surface roughness (R_a) of 1.5 ± 0.5 nm measured by confocal white light microscopy (μSurf, Nanofokus AG, Germany). Close to the sample surfaces, single bubbles were generated in 3.5% NaCl solution which corresponds to a typical seawater salt concentration using the setup shown in Fig. 1 via optical breakdown from a focused nanosecond-long laser pulse (Litron Nd:YAG nano S, wavelength of 532 nm). The pulse was focused into a glass cuvette with PVC bottom (dimensions 50 mm × 50 mm × 50 mm) using a long working distance microscope objective (Mitutoyo, 50x, NA = 0.42), more details on the bubble generation are presented in Ref [32]. This resulted in single bubbles with a maximum radiusR_{max} = 0.5 mm at precisely controllable locations. As part of the metallic body of the microscope objective was in contact with the liquid, it was carefully coated with an insulating silicon to avoid any interference with the electrochemical measurements.

A three-electrode cell was connected to a potentiostat (Gamry Reference 600) in chronoamperometric mode to measure the current through the aluminium wire at open circuit potential (OCP). The main working electrode (WE1) was the aluminium wire subjected to the bubble collapse, the second sample of same material and dimensions was used as the counter electrode (or WE2) and the reference electrode was Ag/AgCl. The main electrode (WE1) was placed perpendicular to the laser beam as sketched in Fig. 1b. This geometric configuration is necessary to avoid spurious signals induced by the plasma, in particular for small stand-off distances from the bubble to the sample [16]. The current between two working electrodes (WE1 and WE2) and the potential of their couple versus the reference electrode were recorded for 2 ms via the dedicated output channels of the potentiostat (“I monitor” and “E monitor”) using an oscilloscope at 100 MHz sampling rate (Teledyne LeCroy HD4096). For optimized frequency response, all internal filters of the potentiostat were turned off [33]. The rise time of the potentiostat is given as smaller than 250 ns by the manufacturer. To estimate the rise time of the entire setup, i.e. including the electrodes, we use the (spurious) chronoamperometric peak that is generated once the laser hits the electrode by a photoeffect [16]. As the laser pulse duration is only about 5 ns it is a good approximation to a Dirac’s delta excitation. Here we take the rise time of the photoinduced current as rise time of the entire system. We find a rise of the electrochemical measurement of 400 ns. To lower the noise from the environment, the potentiostat was grounded and the sampled data is smoothened using a moving average window of 500 ns length.

The sample holder was attached to a translation stage (PI Physik instrument) to adjust the distance between the surface of the sample and the bubble center with sub-micrometer precision using an in-house developed control software. A parametric study on the stand-off distance was performed where the plasma to boundary distance d was varied between 0 and 1 mm. This distance is conveniently expressed using the non-dimensionalized stand-off $\gamma = d/R_{max}$, i.e., $\gamma = 0$ to 2.0. From the high-speed imaging γ is measured geometrically as sketched in Fig. 1d by determining the maximum bubble radius in vertical direction to and away from the solid, as discussed in detail in [33], and the distance d between plasma and solid. We estimate an uncertainty of 10 μm for the measurement of d and R_{max}. Working and counter electrodes (WE1 and WE2 in Fig. 1a) were both attached to the translation stage to maintain a constant distance and measurement geometry.

Two high-speed cameras were used to image the bubble dynamics and stand-off distance. The main camera (Shimadzu HPV-X2) was placed in parallel with the surface of sample (see Fig. 1a) to record the bubble dynamics at frame rates of up to 5,000,000 frames per second (fps). It was equipped with a macro lens (Canon MP-E 65 mm f/2.8 1–5 times magnification) giving a resolution of 7 μm per pixel. The illumination was provided by an LED (SugarCUBE™ Ultra LED Illuminator) in transmitted light. Perpendicular, the second camera (Photron fastcam mini) was operated at 120,000 fps imaging the sample surface (see Fig. 1b). This camera was used to axially align the bubble with the main working electrode (WE1). Illumination was realized via light reflected from the surface of the sample from a second light source (SugarCUBE™ Ultra LED Illuminator). The high-speed imaging was synchronized to the potentiostat with the help of the oscilloscope to record the electrochemical corrosion current and the exposure signals of the high-speed cameras simultaneously. For further synchronization a short rise time photo detector (Thorlabs DET-10A) was used with the oscilloscope to detect the instance of bubble generation.

3. Results and discussion

3.1. Effect of stand-off distance on cavitation damage

The bubble dynamics in general is sensitively stand-off dependent. Therefore, we first carry out a parametric study of the damage as a function of the stand-off γ. To estimate the damage by one single bubble, we integrate the corrosion current over time for the entire bubble dynamics and get the total corrosion charge $Q = \int I(t)dt$. Then, via the Faraday equation, the weight of the newly formed passive layer on the sample can be obtained:

$$\Delta w = \frac{QM}{nF}$$

where Δw is the weight change in grams, Q is the charge in C, M is the molar mass in g/mole (26.98 for Al), n is the number of electrons

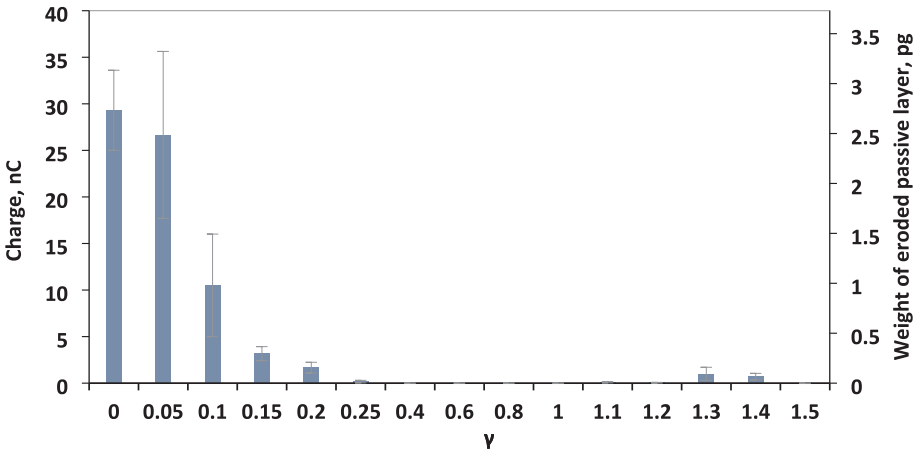

Fig. 2. The obtained charge and the calculated weight of eroded passive layer due to single bubble collapse near the surface of aluminum as a function of γ.

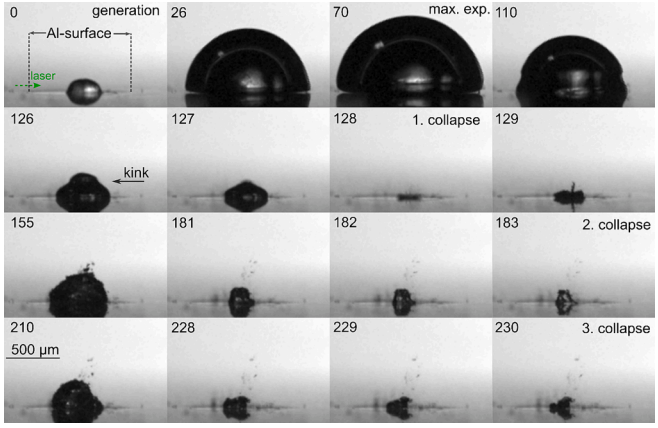

Fig. 3. High speed imaging (1 Mfps) of bubble generation and collapses at $\gamma = 0.10$. The arrow in the first frame shows the direction of laser beam used for bubble seeding. Times are indicated in each frame in microseconds with respect to the bubble generation.

transferring in anodic reaction (n = 3 for Al here) and F is the Faraday constant (95458C/mole). Here we assume that the material removal mainly occurs in the passive film through a skimming mechanism, i.e., layer-like progression induced by the shear stresses. Some weight-lossless plastic deformation in the form of indentation is also expected [6] though this limited plastic deformation could not result in formation of cracks or material removal in the form of detached particles on the surface of ductile aluminium. As the surface will be quickly repassivated after the bubble collapse, the weight loss of the sample due to the removal of passive layer is roughly equal to the weight of elementary aluminium which reacts with oxygen, i.e., Δw in the Faraday equation. Fig. 2 shows the produced charge and the calculated weight of eroded passive layer as a function of the stand-off. At each stand-off at least three measurements were evaluated, and the error bars show the standard deviation of the mean. The calculated weight losses are in the order of few picograms (pg). Clearly, the bubble dynamics are significantly damaging only for $\gamma <\approx 0.25$. This has been previously reported and is a result of shockwave self-focusing during the collapse [6]. The highest damage is found here for $\gamma \approx 0.1$. There, the weight of the re-formed passive layer is about 2.5 pg. To put this into relation, we assume erosion in the shape of a cylindrical hole and calculate the equivalent cylinder radius. We estimate the passive layer thickness as $d = 5\text{nm}$ [34], and calculate $\rho\pi r^2 d = \Delta w = 2.5\text{pg}$, where r is the equivalent radius, and $\rho = 3950\text{kg/m}^3$ the mass density of aluminum oxide. Then we obtain erosion in a hole of radius $r = 6.3$ µm. No damage is detected for $\gamma > 0.25$, only around $\gamma \approx 1.3-1.4$, some minor damage is also detectable, which is in agreement with the trend reported by Philipp and Lauterborn [35].

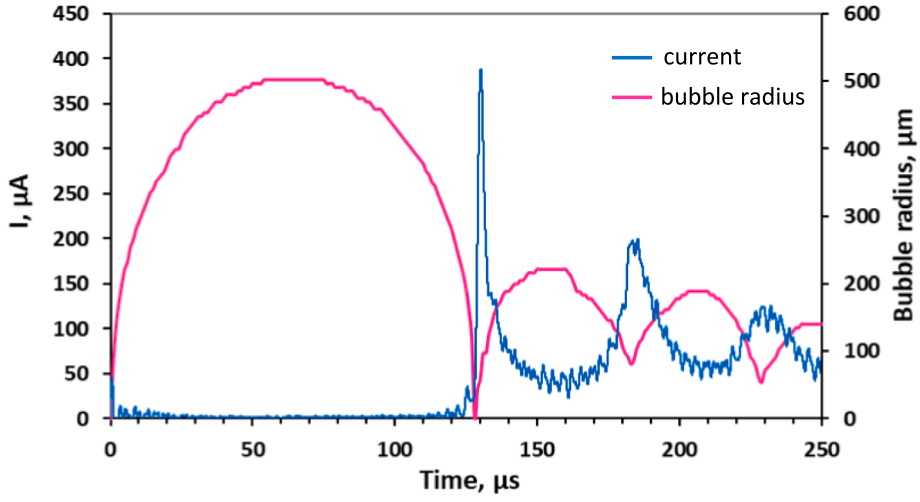

Fig. 4. Bubble radius evolution and corresponding corrosion current as a function of time at $\gamma = 0.10$. The time t = 0 corresponds to the bubble generation.

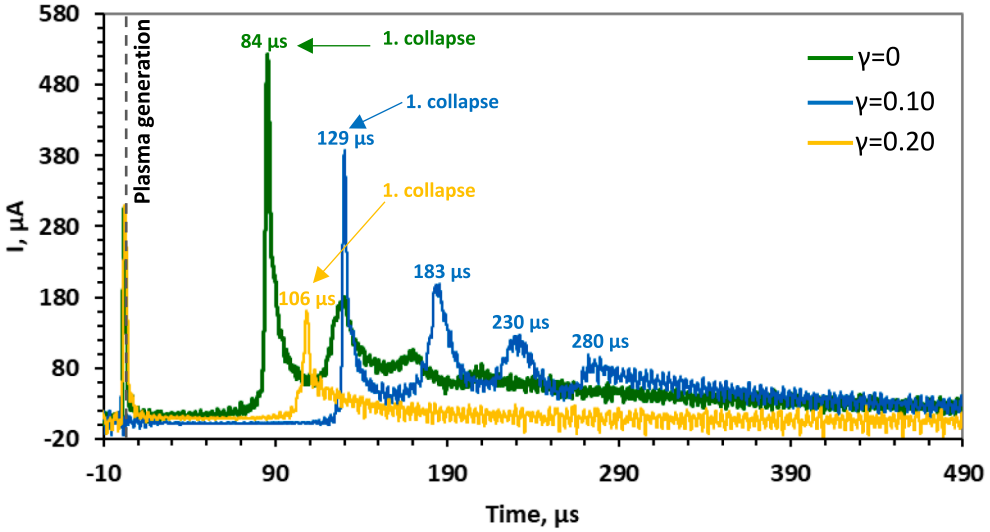

Fig. 5. Time-dependent corrosion current obtained at OCP during the entire bubble dynamics including the bubble generation, collapse, and subsequent rebounds at various γ of 0, 0.10 and 0.20. The time of plasma generation, t = 0, is also included in the figure.

3.2. *Correlation of high-speed imaging with chronoamperometry*

3.2.1. *Damaging stand-off regime*

In the previous section it was shown that the largest damage occurs for $\gamma \rightarrow 0$. A representative bubble dynamics from this regime is shown in Fig. 3 for the stand-off γ = 0.10. The frame times indicated in each frame are given respective to the first frame after bubble generation: t = 0. In the first frame, the plasma is generated, and then the bubble expands. Around t = 70 μs, the bubble has reached its maximum radius of about 0.5 mm in a hemispherical shape. In this stage the pressure inside the bubble is about the water vapour pressure and consequently the bubble starts to collapse. At t = 110 μs, bubble shape has changed, and a kink is formed due to the radial flow toward the axis of symmetry which results in the ejection of a supersonic needle-jet towards the solid [11]. At t = 128 μs the bubble has collapsed; and it subsequently rebounds on the surface now with a maximum diameter of about 400 μm (t = 155 μs). The bubble then starts to collapse another time, and a second collapse is seen at the frame taken at 183 μs. This process is repeated another time and the third collapse occurs at t = 230 μs. All dynamics take part at the solid boundary.

To correlate the bubble dynamics with the chronoamperometric response of the sample, Fig. 4 shows the evolution of the bubble radius $R(t)$ and the respective current between the two identical electrodes at open circuit potential (OCP). The time series covers the entire bubble dynamics including the bubble generation, collapse, and subsequent rebounds (blue). The maximum peak current of 380 μA at $t \approx 128\mu s$ follows directly the instance of the first collapse, i.e., when the bubble radius approaches zero for the first time in Fig. 3. Subsequent collapses are related to smaller amplitudes with somewhat wider peaks. For example, the peak that coincides with the second collapse around t = 183 μs, has an amplitude of about 200 μA. The lower amplitude of the second peak suggests the lower surface damage by the second collapse compared with the first one. The smaller amplitudes are a result of damping which can also be seen in the decreasing amplitudes of the maximum radius in time. We suspect that the peaks get wider for subsequent collapses as the bubble tends to fragment during the first collapse and loses some of its cylindrical symmetry. This can result in an "asynchronous collapse" where parts of the bubble are already collapsing while others are still expanding [6].

After each peak, the corrosion current decreases as the sample repassivates, i.e., the oxide layer on the aluminium surface forms. As this process is a mass transfer limited process that takes some time, the current does not reach zero when the following collapses induce the next peak. From all measurements in our setup, we measure the repassiviation time, i.e. the time until the corrosion current approaches 5% of the peak value, as 195 ± 30 μs. The exact repassivation time may of course depend on the peak amplitude and also the damage geometry on the sample. For example, a deep pit may repassivate at other rate than a planar damage. There are also some other parameters that may affect the repassivation kinetics during the bubble collapse: an increase in the surface temperature, sonochemical decomposition of water into reactive species, and an increase in the mass transfer [36]. In the case of laser induced single bubble collapse, not a significant increase in the temperature of the metallic surface has been observed [37], so this effect can be ignored here. It is true that formation of free radicals inside the plasma can alter the kinetics of chemical reactions inside the solution [38], there are several reasons implying the low priority of these effects during the repassivation after a single bubble collapse. First, it was shown that the bubble does not get in contact with the solid during most of the dynamics. Instead, there is a liquid film between the bubble and the solid [41]. Second, ions are only formed for some tens of nanoseconds within the bubble. During this time, as there is no convection towards the solid, a molecular flow would be necessary to bring a significant amount of ions toward the surface that is not relevant here. Among all phenomena which can affect the repassivation kinetic during the bubble collapse, the increase in mass transfer to the surface by disruption of the interfacial boundary layers can be more significant [36]. This means that oxygen can reach the surface more easily resulting in a higher oxidation rate as compared with a stagnant solution. The increase in the mass transport was also reported to be the main effect of ultrasound on the electrodeposition of metal ions under diffusion control [39]. The values obtained for the repassivation time are consistent with measurements in similar systems. It was reported that the repassivation of an aluminium electrode (kept at a potential of 0 V vs a stainless steel electrode in purified water consisted of 0.1 mol/dm^3 Na_2SO_4) lasts for 100 μs after impingement of a single erodent particle [40,41] and 79 μs under collapse of bubbles generated by ultrasonic source [42]. For UNS S31603 stainless steel, current transients occurred over a short period of time between 18 and 38 ms in a 3.5% NaCl solution [43]. Generally, the repassivation time of various alloys depending on the nature of oxide film, potential of electrode and environment (chemical composition, velocity, and temperature of corrosive medium).

Within the erosive regime, still substantial differences in the time evolution of the corrosion current can be observed. Fig. 5 compares the

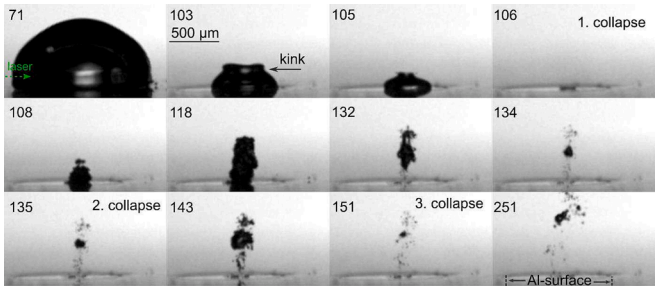

Fig. 6. High speed imaging (1 Mfps) of bubble generation and collapses at $\gamma = 0.20$. Here, only the first collapse occurs at the sample surface. The arrow in the first frame shows the direction of laser beam and times are indicated in each frame with respect to the instance of bubble generation.

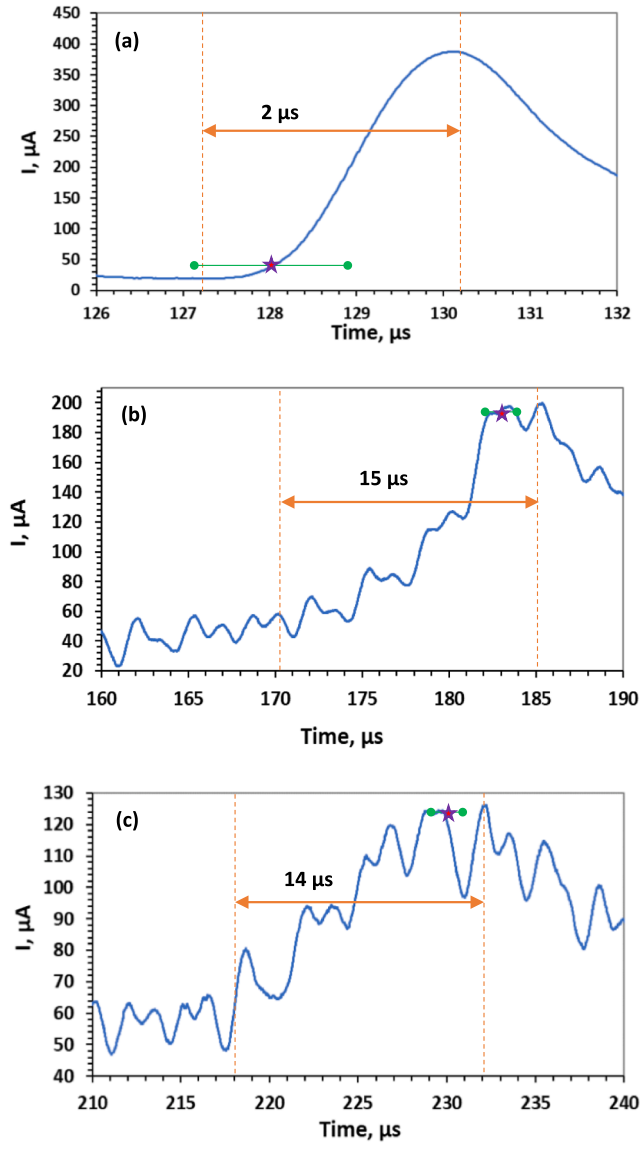

Fig. 7. The details of time-dependent corrosion current obtained at OCP during the bubble collapses at $\gamma = 0.10$: (a) first collapse, (b) second collapse and (c) third collapse. The times when bubbles reach their minimum volume are marked with the stars and the corresponding error bars were included. Please note the different scales.

data from three stand-offs, all within the erosive regime. For example, the (first) collapse peak is larger, the smaller the stand-off. Please take note that for the three measurements the instance of collapse differs because the bubble lifetime, i.e. the time from generation to collapse, is proportional to R_{max} and also a function that is sensitively dependent on γ in this near-wall regime [44,45]. A further difference concerns the value of the plasma generation peak which is largest again for $\gamma = 0$, i.e. when the plasma hits the electrode directly. We would like to mention that not only direct plasma contact produces a current. While at $\gamma = 0.20$ the high-speed imaging clearly confirms that the plasma is not in direct contact with the electrode still a spike is produced at $t = 0$. These signals were attributed to a photo effect on the surface of metals [16] and we will not further evaluate the plasma peaks here. The most interesting observation concerning the bubble dynamics is the difference in the impact of subsequent collapses. While at $\gamma = 0.10$ the second and third collapses are still producing a substantial corrosion current, this is not the case for the slightly larger $\gamma = 0.20$. In the range $0.15 < \gamma \leq 0.25$ we do not find any damage other than from the first collapse. The reasons are revealed in the high-speed imaging in Fig. 6. Before the second collapse, the bubble is pancake-like shaped and then lifts off from the solid boundary. It is ejected into the bulk where the subsequent collapses take part. This corresponding flow fields of this dynamics have been measured and analyzed in [16]. In contrast for $\gamma \leq 0.15$ the subsequent collapses take part directly at the solid.

We close the analysis of the damaging stand-off regime inspecting the electrochemical current peaks at $\gamma = 0.10$ in more details in Fig. 7. The instance of minimum gas phase volume is read from the high-speed imaging and marked by the star symbol, and the horizontal error bars correspond to the interframe time. The first collapse, see Fig. 7a, shows that the peak starts to rise with the instance of minimum bubble volume and has a short rise time of less than 2 µs. We consider this an upper limit, as the rise time is likely limited by the electrical circuitry here. For the second and third collapse the rise time is significantly larger, 15 and 14 µs, respectively, as shown in Fig. 7b and c. High-speed imaging of the bubble in top view of the solid has shown that the gas phase does not reach minimum volume all at once. Instead, when parts of the ring bubble are already in the rebound stage, others are still collapsing. Whereas, this process is particularly fast in the heavily erosive small stand-off case where it takes only about 75 ns, it can take several microseconds during the second collapse because the sphericity of the rebounded bubble is significantly lower and the bubble tends to fragment [6]. Further, it should be considered that after the first collapse the sensor, i.e. the electrode, has changed. After the damage from the first collapse, a passive layer may not have healed completely as this process takes about ≈200 µs (see above), such that the weaker but high wall-shear flows generated during the second collapse damage the pre-damaged surface. Indeed, the thin nascent oxide layer formed on the soft pure aluminium substrate shows a lower resistance against the cavitation-induced stresses as compared to the original passive layer with a higher thickness. Alternatively, the flows from second collapse could increase the repassivation rate by increasing the mass transfer rate which is also detected as an increase in the corrosion current.

3.2.2. *Non-damaging stand-off regime*

Fig. 8 shows a representative dynamics in the non-erosive regime for $\gamma = 0.50$. The respective corrosion current is presented in Fig. 9. The first collapse at t = 112 µs (Fig. 8) is not related with a significant increase in corrosion current in Fig. 9 and thus not damaging. This stand-off is characterized by the regular jet that largely affects the bubble dynamics and shapes the bubble toroidally, see the axial indentation of the upper bubble interface at t = 101 µs. Jet velocities are around 100 m/s and the radius of the jet is about 125 µm, which corresponds to 25% of R_{max}, i.e. the jet is rather thick. This comparably slow and wide jet is known to reduce the collapse strength and prevent shockwave self-focusing and therefore to mitigate cavitation damage [6]. A further detail can be observed in the corrosion current in Fig. 9. The noise is significantly

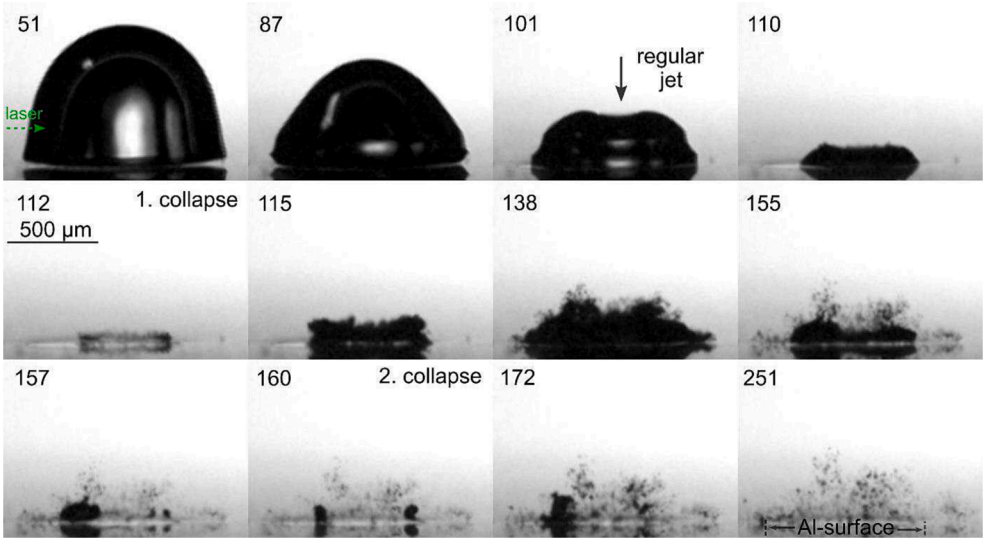

Fig. 8. High speed imaging (1 Mfps) of the bubble generation and collapse at $\gamma = 0.50$. The arrow in the first frame shows the direction of laser beam and times are indicated in each frame with respect to the instance of bubble generation.

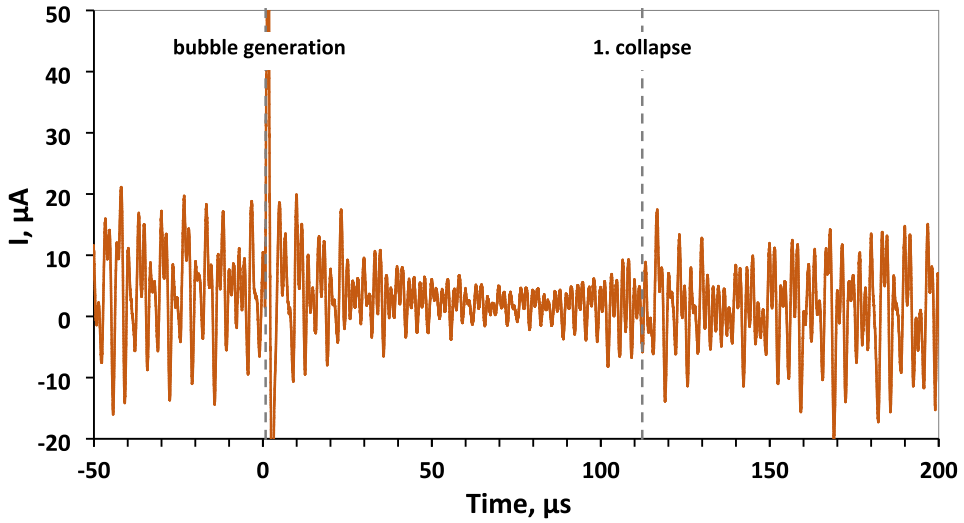

Fig. 9. Time-dependent corrosion current obtained at OCP during the entire bubble dynamics including the bubble generation, collapse, and subsequent rebounds at $\gamma = 0.50$.

reduced as the bubble is expanded over the electrode, see the time span between t = 25 µs to 100 µs. We attribute this to small limited liquid volume between the bubble and the electrode which may induce a depletion of charge carriers in the near-wall region at the electrode and may increase the electrical resistance of the electrochemical arrangement. It is known from dynamic measurements that the liquid layer between bubble and solid is below 15 µm thickness already after about 10 µs but approaches an almost constant value until the jet impacts on the wall [46]. This is further discussed in the Appendix.

3.2.3. Second collapse damaging stand-off regime

Fig. 2 has shown some minor charge and weight loss being produced around $\gamma \approx 1.3-1.4$. The respective high-speed imaging for γ=*1.4* is shown in Fig. 10 and the time-resolved corrosion current in Fig. 11. These data prove three important findings: I) The first collapse, which takes part at some distance from the solid (see t = 105 µs), is not related with any increase in corrosion current. Even though the shock waves emitted are rather strong at this stand-off due to the good sphericity of the bubble, they are emitted apparently too far away from the boundary. II) A regular jet with velocities in the order of 100 m/s pierces the bubble interface at t = 103 µs seen via the indentation in the bubble interface facing the bulk. This jet impacts between 106 µs and 115 µs but does not induce any corrosion current and is not expected to induce damage. III) Instead, some minor damage is only produced during the second collapse around $t = 195\mu s$. This is in agreement with our previous work that showed no damage from the first collapse for $\gamma > 0.25$ but demonstrated the erosive shockwave self-focusing during the second collapse that can result in minor damage [6].

3.3. Summary and discussion

Fig. 12 gives an overview over the different damage regimes identified. It shows the peak amplitudes from first, second, third and fourth collapses. The main erosive regime of the first collapse extends up to $\gamma \approx 0.25$ and decreases for increasing stand-off. When the rebounded bubble collapses in the bulk and not at the solid, the second collapse is not able to produce surface damage ($0.15 < \gamma \leq 0.25$). The small damage produced for $1.1 \leq \gamma \leq 1.4$ is a result of only the second collapse.

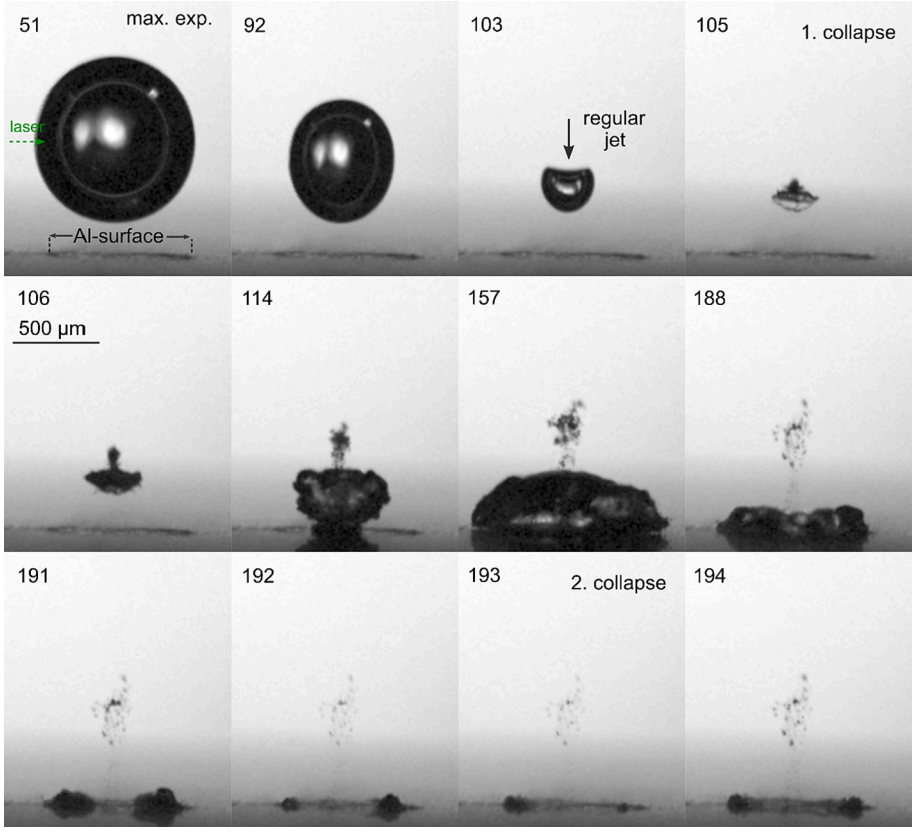

Fig. 10. High speed imaging (1 Mfps) of bubble generation and collapses at $\gamma = 1.4$. The arrow in the first frame shows the direction of laser beam and times are indicated in each frame with respect to the instance of bubble generation.

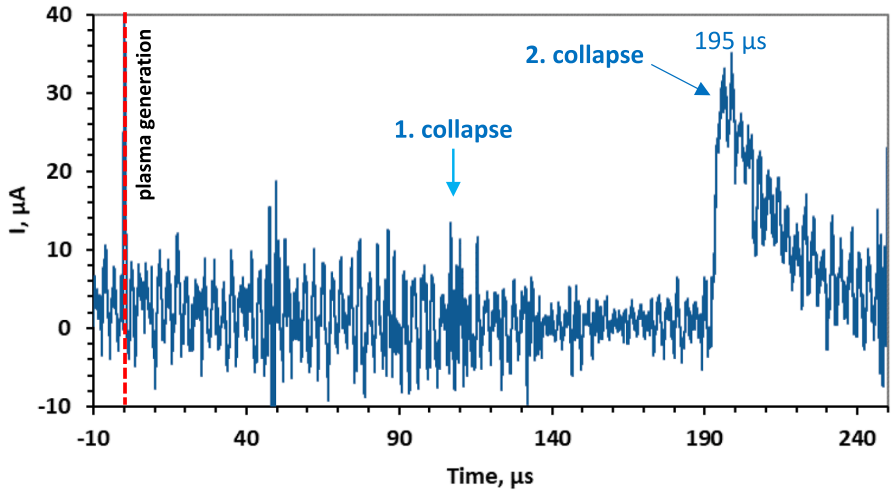

Fig. 11. Time-dependent corrosion current obtained at OCP during the entire bubble dynamics including the bubble generation, collapse, and subsequent rebounds at $\gamma = 1.4$. The time of plasma generation, t = 0, is also included in the figure.

Here, we measured the weight of newly passivated material as about 2.5 pg in the erosive near-wall regime (see Fig. 2). This is about 54 times more than the values reported for a single current time transient on a 250 µm diameter passivated Al electrode in acoustic cavitation by Birkin et al. [47] who reported 46 fg. Considering the differences in the setup the data may still compare well. First, they used a 0.25 mol/dm^3 Na_2SO_4 solution and an electrode potential of + 200 mV versus saturated a calomel electrode (SCE) which could result in different passive layer thickness. Second, they used ultrasonic cavitation induced by a horn resonating at 23.17 kHz but did not employ high-speed imaging, so that the bubble sizes, sphericity and distances to the electrode were unknown. Still from the driving frequency-one can expect a bubble volume that is two orders of magnitude smaller than the bubble generated here. Furthermore, we want to compare our data to the mass erosion rate per single cavitation bubble in a similar setup. Reuter et al. [6] reported volumetric erosion rates in a similar setup obtained by ex-situ confocal profilometry of the eroded volume which translate to 7.76 ng per bubble, using the specific mass density of aluminum as $\rho = 2700 kg/m^3$ from

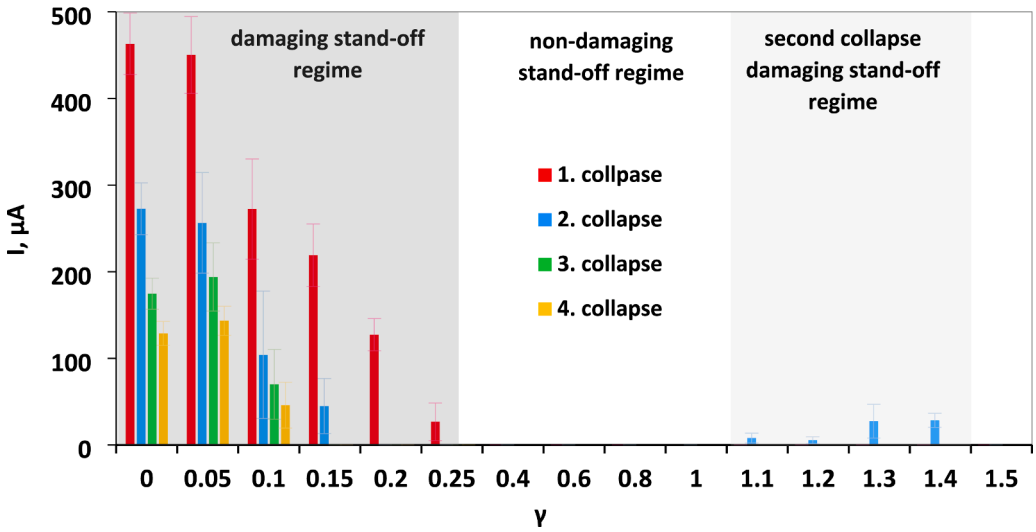

Fig. 12. The maximum amplitude of the current transient peaks during the bubble collapses near the surface of aluminum as a function of γ. No peak was detected for $\gamma = 1.5$ to 2.0 (not shown).

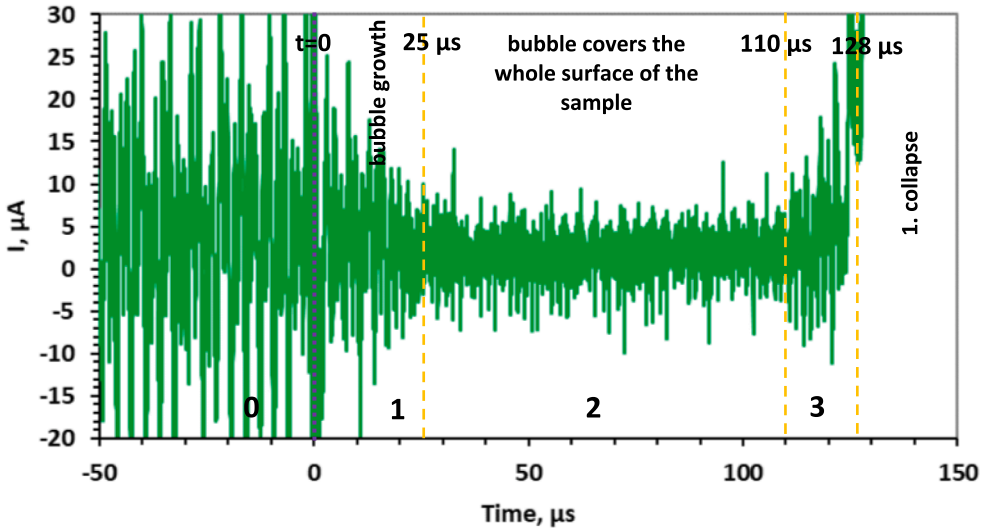

Fig. 13. Comparison of chronoamperometric noise for different expansions of the bubble and before bubble generation (γ = 0.10). As the bubble expands and covers the electrode, the noise is significantly reduced. Here the raw data is presented without digital anti-noise filtering.

the volumetric erosion rates given in that work. This is three orders of magnitude more than the values measured here. This is because here we obtain the weight of the repassivation layer rather than the total erosion. Furthermore, this provides a lower boundary of the weight of the newly formed passive layer because cathodic reactions may occur already on the undamaged material of the sample electrode, such that the charges do not reach the electrometer of the potentiostat. We tried to diminish this effect by using small area electrodes. Still, the striking differences in 2.5 pg /7.76 ng = 3 orders of magnitude give insight into the erosion processes. The mechanical detachment rate is much larger than the repassivation rate. This suggests that the ablation hits into the bulk metallic material rather than ablating oxide layers in large areas and material removal at the one instance of time rather than in an areal pattern. In contrast, a removal of the passive layer in layer-like progression or step by step would result in the formation of orders of magnitude more passive layer during the process.

The strength of the method presented concerns the ability to resolve the small weight fraction on the order of 2.5 pg even at a (sub-) microsecond resolution, for which hardly alternative methods that allow the in-situ measurements in this wet environment. Furthermore, it allows the time-resolved measurement of cavitation damage with a resolution much better than the duration of the bubble dynamics. This way, the damage can be attributed to a specific part of the bubble dynamics and the effect of subsequent collapses can be quantified. Here, the measurements were sensitive enough to record the corrosion current at open circuit potential, i.e. non-invasively. The application of a certain potential to the sample electrode would increase the signal but at the cost of altering the passive layer formation.

4. Conclusions

We showed high-speed time-resolved measurements of the cavitation damage by single laser induced bubble by monitoring the induced corrosion current on an aluminum sample. The response time of the measurement method was much faster than the bubble lifetime and thus together with synchronous high-speed imaging of the bubble dynamics,

correlation between bubble dynamics and surface damage was possible.

The first bubble collapse is by far the most erosive impact and it is only erosive in a small range of stand-offs of $\gamma \leq 0.25$, i.e. when the bubble dynamics take part directly at the boundary as reported before [6]. Subsequent collapses induce increased corrosion rates only if they take part at the surface. For example, some minor damage was found in the range ($1.1 \leq \gamma \leq 1.4$) from the second collapse. Within the erosive regime only for stand-offs $\gamma \leq 0.15$ also the second collapse increases erosion rates, while for $\gamma = 0.20 \text{and} 0.25$ the bubble is ejected from the solid and subsequent collapses occur in the bulk at some distance and thus are not able to increase the corrosion rate. Recently, it was shown from the spatial correlation and bubble dynamics that the regular jet does not induce erosion [6]. Here, from time-resolved measurements we find that the regular jet indeed does not induce damage and even does not significantly increase corrosion. Collapse shock waves, if emitted at some distance from the substrate, are also not correlated with increased corrosion.

The real time detection of the occurrence of erosive cavitation can be challenging in large scale systems. Among the non-invasive techniques, the optical inspection may not be possible as relevant surfaces may be covered by cavitation structures or optically not accessible at all. The interpretation of cavitation noise for damage detection often needs considerable experience and may depend on the exact cavitation system and geometry. Here, electrochemical methods offer a solution. The non-invasive implementation here at open circuit potential (OCP) proven sensitive enough for a real-time detection of cavitation induced damage.

CRediT authorship contribution statement

Morteza Abedini: Conceptualization, Writing – original draft. **Stefanie Hanke:** Conceptualization, Writing – review & editing. **Fabian Reuter:** Conceptualization, Writing – review & editing.

Declaration of Competing Interest

The authors declare that they have no known competing financial interests or personal relationships that could have appeared to influence the work reported in this paper.

Acknowledgements

We would like to acknowledge the German Academic Exchange Service (DAAD) who provided the financial support under the funding ID 57552334. We are indebted to Prof. Claus-Dieter Ohl (chair of Soft Matter, Otto-von-Guericke University Magdeburg) for his support of the work and access to the laboratories. We thank Robert Mettin from University of Göttingen for lending us some of the laser equipment and the potentiostat. We also thank Christina Lopez de Arcaute y Lozano (Materials Science and Engineering, University of Duisburg-Essen) for preparing the samples.

Appendix

In Fig. 13 the raw electrode current, i.e. without any filtering, is shown before the bubble generation ($t = 0$) and during its first oscillation phase. Now looking only at the noise, the curve can be divided into four regions. At region 0 the noise is largest, for 1 it is decreasing, for 2 it is lowest, and for 3 it is increasing again. We explain this with the bubble covering the electrode area. Between 0 μs and $\approx 25\mu s$, the bubble only partly but increasingly covers the electrode area, while between about 25 μs and about 110 μs, the bubble almost covers the entire electrode surface even though there remains a thin liquid film between bubble and solid surface. For $\gamma \geq 0.5$, Reuter and Kaiser [46] measured its thickness d and offered a phenomenological fit as $\mathrm{d}(\gamma) = 29.2\ \mu\mathrm{m}\ \gamma^{4.86} + 4.74\ \mu\mathrm{m}$. We extrapolate the fit to estimate the film thickness at the instance of jet impact for the shown case of $\gamma = 0.1$ and find $d = 4.7\mu m$. There are no signs of film rupturing during the bubble dynamics before the first collapse neither from the high-speed imaging nor from the electrochemical corrosion current and we can expect the film to be on the order of 10 μm during the entire dynamics when the bubble covers the electrode area ($t > \approx 25\mu s$). The thickness of the diffusion layer of oxygen on the surface of aluminium is in the order of 100 μm [48], i.e. significantly reduced by displacement of the bubble. In addition, the electrical resistance between the electrodes may be increased at small gaps. These findings suggest that electrochemical microscopy [49], i.e., the monitoring of reaction rates as a function of the gap width above an electrode may be even feasible in this high-speed arrangement and provide further insights into the bubble dynamics in dedicated experiment.

References

[1] ASTM G32: Standard Test Method for Cavitation Erosion Using Vibratory Apparatus. 2009, ASTM International.
[2] N.D. Shutler, R.B.M., A photographic study of the dynamics and damage capabilities of bubbles collapsing near solid boundaries, J. Basic Eng. 87 (2) (1965) 511–517.
[3] Y. Tomita, A. Shima, Mechanisms of impulsive pressure generation and damage pit formation by bubble collapse, J. Fluid Mech. Cambridge Core 169 (-1) (1986) 535.
[4] A. Philipp, W. Lauterborn, Cavitation erosion by single laser-produced bubbles, J. Fluid Mech. 361 (1998) 75–116.
[5] J.-C. Isselin, A.-P. Alloncle, M. Autric, On laser induced single bubble near a solid boundary: Contribution to the understanding of erosion phenomena, J. Appl. Phys. 84 (10) (1998) 5766–5771.
[6] F. Reuter, C. Deiter, C.-D. Ohl, C.-D. Ohl, Cavitation erosion by shockwave self-focusing of a single bubble, Ultrason. Sonochem. 90 (2022) 106131.
[7] T. Amann, M. Waidele, A. Kailer, Analysis of mechanical and chemical mechanisms on cavitation erosion-corrosion of steels in salt water using electrochemical methods, Tribol. Int. 124 (April) (2018) 238–246.
[8] S. Hong, Y. Wu, J. Zhang, Y. Zheng, Y. Qin, J. Lin, Effect of ultrasonic cavitation erosion on corrosion behavior of high-velocity oxygen-fuel (HVOF) sprayed near-nanostructured WC – 10Co – 4Cr coating, Ultrason. Sonochem. 27 (2015) 374–378.
[9] J. Basumatary, R.J.K. Wood, Different methods of measuring synergy between cavitation erosion and corrosion for nickel aluminium bronze in 3.5% NaCl solution, Tribol. Int. 147 (2020) 104843.
[10] M. Abedini, F. Reuter, S. Hanke, Corrosion and material alterations of a CuZn38Pb3 brass under acoustic cavitation, Ultrason. Sonochem. 58 (January) (2019) 104628.
[11] J. Ryl, J. Wysocka, P. Slepski, K. Darowicki, Instantaneous impedance monitoring of synergistic effect between cavitation erosion and corrosion processes, Electrochim. Acta 203 (2016) 388–395.
[12] S. Hong, Y. Wu, J. Zhang, Y. Zheng, J. Lin, Synergistic effect of ultrasonic cavitation erosion and corrosion of WC-CoCr and FeCrSiBMn coatings prepared by HVOF spraying, Ultrason. Sonochem. 31 (2016) 563–569.
[13] M. Abedini, H.M. Ghasemi, Electrochemical noise and polarization analyses on corrosion of Al-brass alloy during erosion-corrosion, J. Bio- Tribo-Corr. 7 (2) (2021) 1–13.
[14] F. Mohammadi, J. Luo, B. Lu, A. Afacan, Single particle impingement current transients for prediction of erosion-enhanced corrosion on 304 stainless steel, Corros. Sci. 52 (7) (2010) 2331–2340.
[15] G.T. Burstein, K. Sasaki, Detecting electrochemical transients generated by erosion–corrosion, Electrochim. Acta 46 (24–25) (2001) 3675–3683.
[16] F. Reuter, C. Cairós, R. Mettin, Vortex dynamics of collapsing bubbles: Impact on the boundary layer measured by chronoamperometry, Ultrason. Sonochem. 33 (2016) 170–181.
[17] P.R. Birkin, S. Silva-Martinez, A study on the effect of ultrasound on electrochemical phenomena, Ultrason. Sonochem. 4 (2) (1997) 121–122.
[18] P.R. Birkin, T.M. Foley, J.L. Barber, H.L. Martin, Microsecond resolution of cavitation bubble dynamics using a high-speed electrochemical impedance approach, Chem. Commun. 52 (76) (2016) 11406–11409.
[19] P.R. Birkin, R. O'Connor, C. Rapple, S. Silva Martinez, Electrochemical measurement of erosion from individual cavitation events generated from continuous ultrasound, J. Chem. Soc. Faraday Trans. 94 (22) (1998) 3365–3371.
[20] P.R. Birkin, D.G. Offin, P.F. Joseph, T.G. Leighton, Cavitation, shock waves and the invasive nature of sonoelectrochemistry, J. Phys. Chem. B 109 (35) (2005) 16997–17005.

[21] P.R. Birkin, D.G. Offin, T.G. Leighton, Electrochemical measurements of the effects of inertial acoustic cavitation by means of a novel dual microelectrode, Electrochem. Commun. 6 (11) (2004) 1174–1179.
[22] P.R. Birkin, et al., Investigation of noninertial cavitation produced by an ultrasonic horn, J. Acoust. Soc. Am. 130 (2011) 3297.
[23] P.R. Birkin, J.F. Power, M.E. Abdelsalam, T.G. Leighton, Electrochemical, luminescent and photographic characterisation of cavitation, Ultrason. Sonochem. 10 (4-5) (2003) 203–208.
[24] P.R. Birkin, S. Silva-martinez, Determination of heterogeneous electron transfer kinetics in the presence of ultrasound at microelectrodes employing sampled voltammetry, Anal. Chem. 69 (11) (1997) 2055–2062.
[25] P.R. Birkin, S. Silva-Martinez, A study of the effect of ultrasound on mass transport to a microelectrode, J. Electroanal. Chem. 416 (1-2) (1996) 127–138.
[26] P.R. Birkin, E. Watson, T.G. Leighton, Efficient mass transfer from an acoustically oscillated gas bubble, Chem. Commun. (2001) 2650–2651.
[27] D.G. Offin, P.R. Birkin, T.G. Leighton, An electrochemical and high-speed imaging study of micropore decontamination by acoustic bubble entrapment, PCCP 16 (2014) 4982–4989.
[28] E. Maisonhaute, P.C.W., R.G. Compton, Surface acoustic cavitation understood via nanosecond electrochemistry, J. Phys. Chem. B 105 (2001) 12087–12091.
[29] R.W. Revie, H.U. Herbert, Corrosion and Corroison Control: An Introduction to Corrosion Science and Engineering, fourth ed., A John Wiley & Sons INC., 2008.
[30] B. Johnson, et al., Using ellipsometry and x-ray photoelectron spectroscopy for real-time monitoring of the oxidation of aluminum mirrors protected by ultrathin MgF2 layers. Astronomical Optics: Design, Manufacture, and Test of Space and Ground Systems II, SPIE, 2019.
[31] G. Cheek, et al., Passive Film characterization on aluminum by impedance spectroscopy. NACE Corrosion, 2002.
[32] F. Reuter, C.-D. Ohl, Supersonic needle-jet generation with single cavitation bubbles, Appl. Phys. Lett. 118 (2021), 134103.
[33] R.M. Fabian Reuter, Electrochemical wall shear rate microscopy of collapsing bubbles, Phys. Rev. Fluids 3 (2018), 063601.
[34] J. Evertsson, F. Bertram, F. Zhang, L. Rullik, L.R. Merte, M. Shipilin, M. Soldemo, S. Ahmadi, N. Vinogradov, F. Carlà, J. Weissenrieder, M. Göthelid, J. Pan, A. Mikkelsen, J.-O. Nilsson, E. Lundgren, The thickness of native oxides on aluminum alloys and single crystals, Appl. Surf. Sci. 349 (2015) 826–832.
[35] M. Dular, O.C. Delgosha, M. Petkovšek, Observations of cavitation erosion pit formation, Ultrason. Sonochem. 20 (4) (2013) 1113–1120.
[36] B.G. Pollet (Ed.), Power Ultrasound in Electrochemistry: From Versatile Laboratory tool to Engineering Solution, John Wiley & Sons, 2012.
[37] S.A. Beig, B. Aboulhasanzadeh, E. Johnsen, Temperatures produced by inertially collapsing bubbles near rigid surfaces, J. Fluid Mech. 852 (2018) 105–125.
[38] F.G.F.Q. Kewen Peng, R. Jiang, Q.u. Wanjun, Q. Wang, Production and dispersion of free radicals from transient cavitation Bubbles: An integrated numerical scheme and applications, Ultrason. Sonochem. 88 (2022), 106067.
[39] M.E. Hyde, R.G. Compton, How ultrasound influences the electrodeposition of metals, J. Electroanal. Chem. 531 (1) (2002) 19–24.
[40] P.R. Birkin, J.L.B., Particle induced surface erosion–Tumbling and direct impact; a high-speed electrochemical, acoustic and visual study, Wear 428–429 (2019) 147–153.
[41] P.R. Birkin, R. Lear, L. Webster, L. Powell, H.L. Martin, In-situ detection of single particle impact, erosion/corrosion and surface roughening, Wear 464-465 (2021) 203527.
[42] P.R. Birkin, et al., Microsecond resolution of cavitation bubble dynamics using a high-speed electrochemical impedance approach, Chem. Commun. 52 (2016) 11406.
[43] S.S. Rajahram, T.J. Harvey, R.J.K. Wood, Electrochemical investigation of erosion – corrosion using a slurry pot erosion tester, Tribol. Int. 44 (3) (2011) 232–240.
[44] W.L. Christiane Lechner, M. Koch, R. Mettin, Jet formation from bubbles near a solid boundary in a compressible liquid. Numerical study of distance dependence, Phys. Rev. Fluids 5 (2020), 093604.
[45] F. Reuter, Q. Zeng, C.-D. Ohl, The Rayleigh prolongation factor at small bubble to wall stand-off distances, J. Fluid Mech. 944 (2022).
[46] S.A.K. Fabian Reuter, High-speed film-thickness measurements between a collapsing cavitation bubble and a solid surface with total internal reflection shadowmetry, Phys. Fluids 31: (2019) 097108.
[47] Vian, C.J.B., P.R. Birkin, and T.G. Leighton, Opto-isolation of electrochemical systems in cavitation environments. 2009. **37**(12): p. 5064-5069.
[48] Y.L. Cheng, Z. Zhang, F.H. Cao, J.F. Li, J.Q. Zhang, J.M. Wang, C.N. Cao, A study of the corrosion of aluminum alloy 2024–T3 under thin electrolyte layers, Corros. Sci. 46 (7) (2004) 1649–1667.
[49] G. Wittstock, M. Burchardt, S. Pust, Y. Shen, C. Zhao, Y.S. Pust, C. Zhao, Scanning electrochemical microscopy for direct imaging of reaction rates, Angew. Chem. Int. Ed. Engl. 46 (10) (2007) 1584–1617.